applied sciences

MDPI

Article

Study on Dynamic Loading Characteristics of Rock Containing Holes

Chuanwei Zang [1], Qi Li [1], Miao Chen [1,*], Xiaoshan Wang [2], Can Xiao [1] and Hongyuan Tu [1]

[1] College of Energy and Mining Engineering, Shandong University of Science and Technology, Qingdao 266590, China; chuanweizang@163.com (C.Z.); lq15689949981@163.com (Q.L.); xc76580@163.com (C.X.); rhq114514@163.com (H.T.)
[2] School of Science, Qingdao University of Technology, Qingdao 266590, China; wangxiaoshan@qut.edu.cn
* Correspondence: miaochen@sdust.edu.cn; Tel.: +86-19511628958

Abstract: Accurately characterizing the mechanical behavior and fracture mechanisms of rock containing holes under dynamic loads is essential for ensuring the stability of underground rock structures. In this study, to enhance the understanding of the fracture processes in rock specimens with cavities subjected to dynamic impacts, experimental and numerical studies focusing on the influence of borehole geometry and strain rate are conducted. The results reveal that the strain rate affects the specimens' dynamic mechanical strength and peak strain. However, the degree of such influence diminishes as the borehole diameter increases in specimens containing two holes. Fractures that lead to failure are primarily initiated at the axial and radial edges of the holes, the specimen extremities, and around the rock bridges in specimens with dual cavities, indicating significant stress concentration zones within the stress field distribution for specimens with a single hole. Further analysis using displacement field diagrams confirms that shear-induced fractures are the predominant cause of failure across all specimens. These findings provide critical insights for developing borehole pressure relief technology to protect against the risks of deep dynamic impacts.

Keywords: rock material; specimen containing holes; dynamic mechanical parameters; failure modes; displacement field

check for updates

Citation: Zang, C.; Li, Q.; Chen, M.; Wang, X.; Xiao, C.; Tu, H. Study on Dynamic Loading Characteristics of Rock Containing Holes. *Appl. Sci.* **2024**, *14*, 3395. https://doi.org/10.3390/app14083395

Academic Editor: Tiago Miranda

Received: 13 March 2024
Revised: 10 April 2024
Accepted: 11 April 2024
Published: 17 April 2024

Copyright: © 2024 by the authors. Licensee MDPI, Basel, Switzerland. This article is an open access article distributed under the terms and conditions of the Creative Commons Attribution (CC BY) license (https://creativecommons.org/licenses/by/4.0/).

1. Introduction

The increasing demand for resources has led to deeper mining operations, which encounter greater challenges and more frequent dynamic disasters, such as rockbursts [1,2]. These incidents are notable for their suddenness and high destructive potential [3–7], significantly hindering the progress of scientific and efficient practices in deep coal mining. Current strategies emphasize early warning systems and rock mass control technologies to counteract these events. Early warning mechanisms deploy a variety of monitoring techniques to assess potential risks, incorporating methods such as drill cuttings analysis, deformation monitoring, microseismic (MS) monitoring [8–11], and advanced seismic wave speed imaging [12,13], alongside acoustic emission (AE) and electromagnetic radiation (EMR) technologies [14,15]. The synergy of these methods enhances the predictive capabilities for rockburst occurrences. Meanwhile, rock mass control involves strategies like local pressure relief [16–20] and reinforcement of the surrounding rock [21,22]. Among these, borehole pressure relief technology [23–25] is particularly effective in stress redistribution within coal and rock masses in high-stress areas, due to its quick results, cost-effectiveness, and ease of application. This technology is especially beneficial in preventing deformations in rock masses in areas vulnerable to rockbursts.

Given the complex on-site conditions and the need to minimize operational disruptions, research on borehole pressure relief technology often begins with controlled indoor experiments to validate its effectiveness before proceeding to field engineering tests. This method has prompted many scholars to study the dynamic cracking processes, failure

mechanisms, and mechanical properties of rocks under borehole pressure relief through experimental investigation. For example, Chen et al. [26] explored the correlation between borehole parameters and rock mechanical properties, deducing that enlarging sections and reducing the spacing between holes can mitigate the formation of lateral fractures, thereby lowering the risk of slabbing in practical applications. Similarly, Lin et al. [27] examined the impact of random and structured hole distributions on crack initiation, coalescence, and the failure patterns of rock materials, subsequently suggesting a criterion based on hole distribution. Furthermore, Li et al. [28] assessed the efficacy of boreholes with varying diameters compared to those with uniform diameters, revealing that boreholes with fluctuating diameters significantly enhance pressure relief more effectively than uniform diameter boreholes with the same maximum diameter.

This research significantly advances our understanding of damage in flawed rock materials, proving to be a crucial asset for engineering applications. With technological progress, the Split Hopkinson Pressure Bar (SHPB) method has become the preferred technique for studying rock materials' mechanical behavior and fracture mechanisms at high strain rates. Many scholars [29–32] have applied SHPB technology to investigate the mechanical characteristics of flawed rocks. For instance, Zou et al. [33] performed dynamic impact tests on flawed rock materials to discern the variance in degradation mechanisms under quasi-static loading conditions. Similarly, Li et al. [34] analyzed the dynamic failure modes of rocks with single and double flaws, identifying nine distinct fracture types that occur during the failure process of rocks. Moreover, You et al. [35], among others, utilized SHPB experiments to study rock materials under various loading conditions, demonstrating a distinct dependence of mechanical response and cracking mechanisms on strain rate. Additionally, Li et al. [36–38] found that rock specimens with cavities tend to exhibit shear fractures at high impact velocities, while tensile fractures are more common at lower velocities.

The insights gained from the referenced studies stem from a combination of indoor experiments and numerical simulations, each with its own set of advantages and drawbacks. The variability in the composition of rock materials might influence the results of indoor experiments, and utilizing high-speed cameras to analyze the dynamic failure process of rocks may not fully reveal the underlying mechanisms. The Discrete Element Method (DEM) model [39,40] addresses these challenges by enabling the continuous monitoring of cracking patterns throughout the loading process. Researchers have widely adopted this method to study rock fracture mechanisms, demonstrating its efficacy in precisely depicting the dynamic fracture behaviors of rocks [41,42].

Despite considerable research on the mechanical behaviors and crack development in rocks and similar brittle materials with cavities, the specifics of rock loading under diverse conditions are not fully comprehended, largely because of a concentration on static loading in the literature. This study employs Split Hopkinson Pressure Bar (SHPB) testing for rock specimens with cavities. After laboratory experiments, a numerical SHPB system, simulated via DEM coding, is created, with its micro-level parameters carefully adjusted to match empirical observations. This research investigates the effects of strain rates and cavity parameters on the rock specimens' dynamic mechanical attributes and breakdown mechanisms. Ultimately, it seeks to deepen our understanding of the dynamic loading phenomena in rock materials with cavities, thereby offering detailed insights into their structural behavior under different stress scenarios.

2. Numerical Model

2.1. Experimental Equipment and Data-Processing Methods

As depicted in Figure 1, dynamic mechanical experiments were conducted on specimens using the Split Hopkinson Pressure Bar (SHPB) apparatus. The terminal surfaces of the rock specimens were polished to ensure uniform contact before positioning them between the incident and transmission bars of the SHPB system. A high-speed camera documented the deformation and fracture dynamics of the specimens during the testing period.

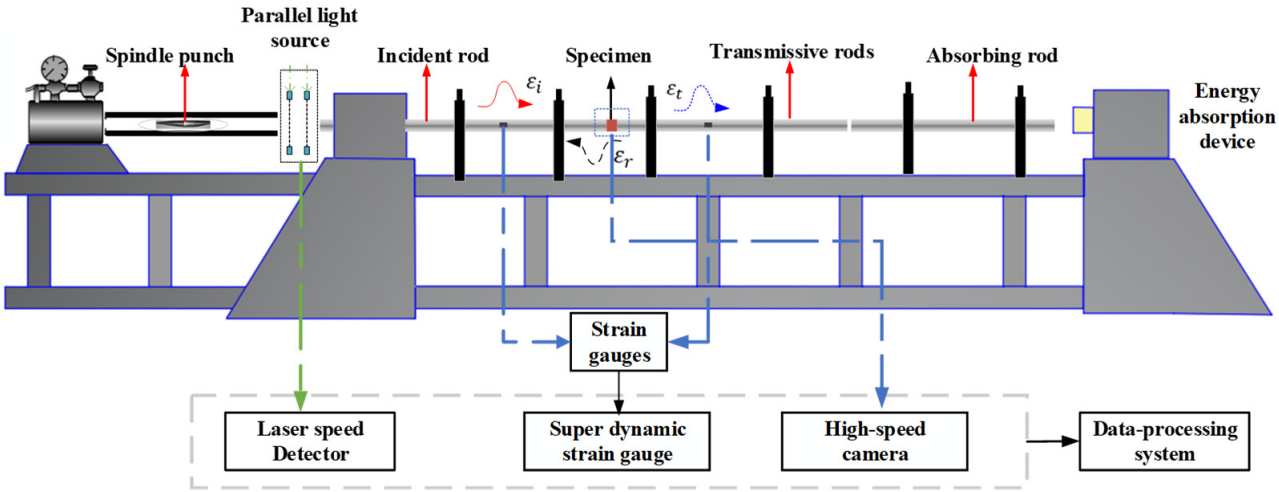

Figure 1. Schematic diagram of the SHPB system.

After the dynamic impact test was concluded, the stress ($\sigma_s(t)$), axial strain ($\varepsilon_s(t)$), and strain rate $(\dot{\varepsilon}_s(t))$ for the specimens were determined using the stress uniformity theory and the three-wave method, as detailed in Equations (1)–(3). Here, A_0, C_0, and E_0 symbolize the cross-sectional area of the pressure bar (m), the velocity of the elastic longitudinal wave (m/s), and the elastic modulus of the waveguide bar (GPa), respectively. The variables $\varepsilon_I(t)$, $\varepsilon_R(t)$, and $\varepsilon_T(t)$ represent the three types of electrical signals generated. Furthermore, A_1, I_0, and t are used to denote the specimen's cross-sectional area (m^2), length (m), and the time span of the dynamic loading, respectively.

$$\sigma_s(t) = E_0A_0/2A_1 - \varepsilon_R(t) - \varepsilon_T(t) \quad (1)$$

$$\varepsilon_s = C_0/l_0\int_0^{t_0}(\varepsilon_I(t) - \varepsilon_R(t) - \varepsilon_T(t))dt \quad (2)$$

$$\dot{\varepsilon} = C_0/l_0(\varepsilon_I - \varepsilon_R - \varepsilon_T) \quad (3)$$

Sandstone, widely recognized as the prevalent type of material in underground engineering, was selected and shaped into cylindrical specimens measuring 50 mm in diameter and 50 mm in height using professional cutting tools. The deviation in parallelism and perpendicularity of the end surfaces of each specimen was maintained below 0.02 mm, meeting the International Society for Rock Mechanics' (ISRM) criteria for surface flatness. The key mechanical properties measured were a density of 2570 kg/m^3, an elastic modulus of 8.7 GPa, and a Poisson's ratio of 0.23.

To ensure the experimental results' precision, it is critical that the specimen's ends reach dynamic stress equilibrium, as demonstrated by the close alignment of stress history data at both ends during the impact sequence [43]. Figure 2 shows a schematic diagram of the action of a dynamic stress wave. Figure 3 depicts the stress–time curve for a specimen featuring a single 8 mm hole exposed to a strain rate of 100 s^{-1} in an indoor dynamic loading test. The diagram shows that the stress numerical curves at the incident (I_n + R_e) and transmitted (T_r) ends converge, virtually superimposing on each other. This overlap suggests that the specimen achieved a dynamic equilibrium state, thus confirming the accuracy of the numerical findings derived from the experiment.

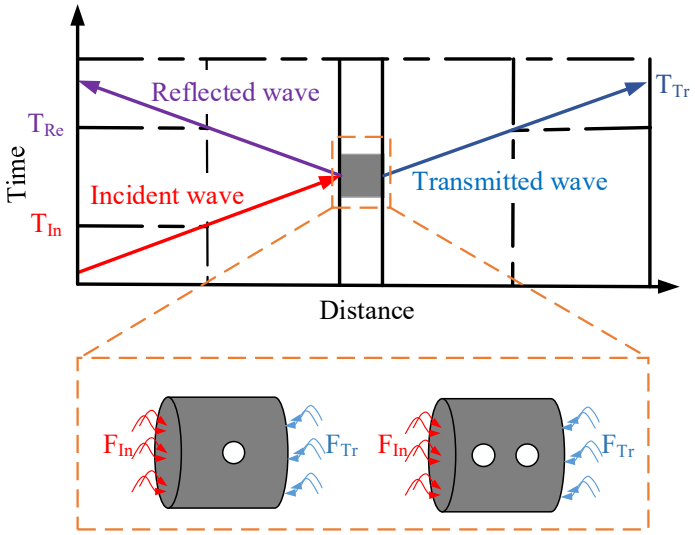

Figure 2. Schematic diagram of dynamic stress wave action.

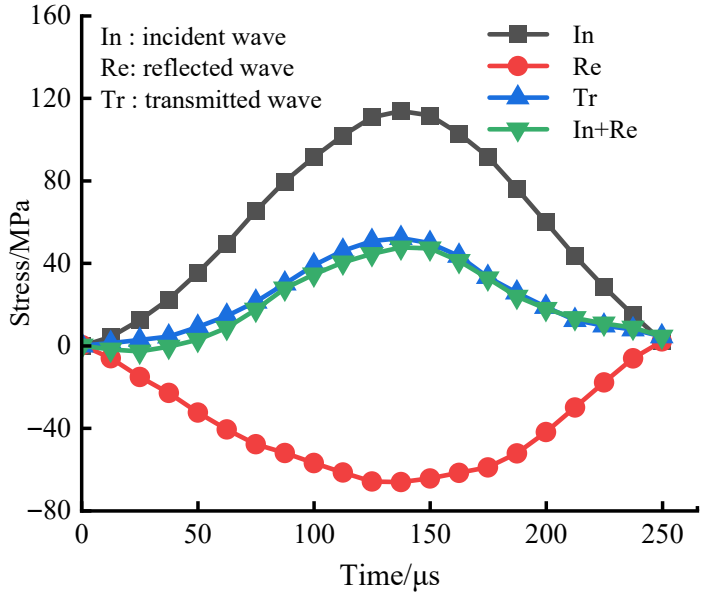

Figure 3. Dynamic equilibrium state inspection.

2.2. Introduction to the Discrete Element Method and the Bonded Particle Model

In 1979, Cundall and Strack initiated the development of the Discrete Element Method (DEM) [44], establishing the basis for the Particle Flow Code (PFC). PFC simulations replicate the mesoscopic mechanical behavior of rocks by treating each particle as an independent computational entity, emphasizing the interactions and evolving dynamics at particle contacts. This method allows for a precise representation of mechanical failures observed in the macroscopic failure stages of rocks. By integrating various parameters from the specimen's failure process, PFC adeptly models the formulation of failure equations, accurately capturing discontinuities like cracking and separation. Such simulations reflect the fundamental mechanisms, procedures, and outcomes associated with rock mechanical failures, thus enabling their comparison and verification against field experiments. As a result, researchers increasingly utilize PFC to explore the mechanical attributes of discontinuous materials and the fracture behaviors of continuous media.

PFC incorporates two primary bonding models: the Contact Bond Model (CBM) and the Parallel Bond Model (PBM). The CBM cannot resist frictional forces at the bonding interface, presenting only bonded and unbonded states without opposing relative rotation.

In contrast, the PBM operates like a collection of springs with both standard and shear stiffness, allowing it to withstand frictional forces and support the transfer of forces and moments. When the strength threshold is surpassed, the bond model fails, and the PBM temporarily resembles a linear model, As shown in Figure 4. This study employs PFC2D to replicate the mesoscopic mechanical behaviors and crack formation in rock masses containing voids under dynamic impact. Previous research suggests that the PBM yields more accurate results for homogeneous materials like rock [45], which has led to the selection of the PBM viscous model for this numerical analysis.

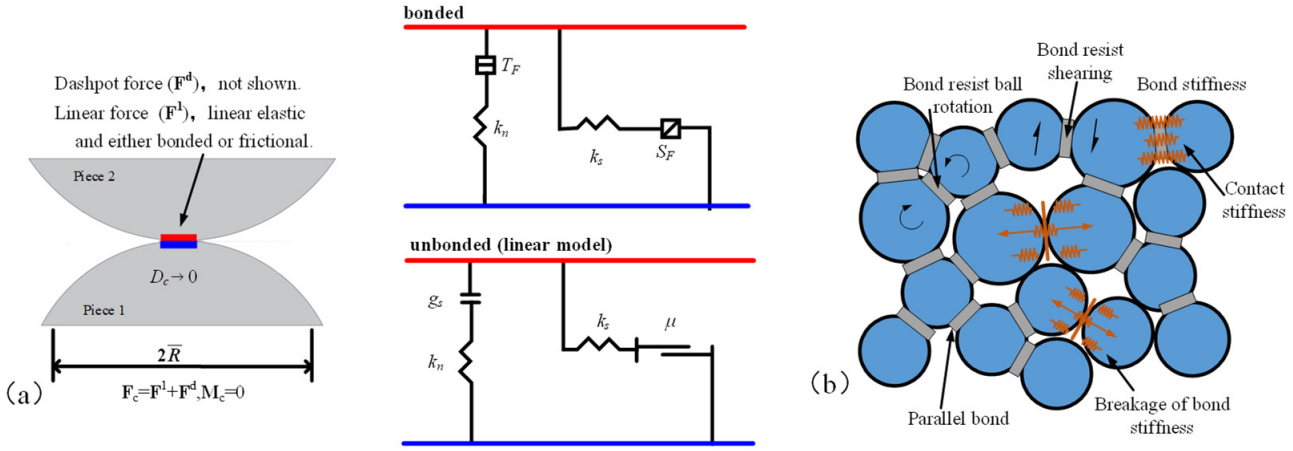

Figure 4. Behavior and rheological components of the (**a**) Contact Bond Model; (**b**) Parallel Bond Model (PBM).

2.3. Numerical Model of the Split Hopkinson Pressure Bar System

In this study, a dynamic uniaxial Split Hopkinson Pressure Bar (SHPB) setup utilizing Particle Flow Code in 2 Dimensions (PFC2D) was constructed, as depicted in Figure 5. This setup includes three main elements: a striker bar, an incident bar, and a transmission bar, with lengths of 300 mm, 1500 mm, and 800 mm, respectively. To facilitate uniform stress wave transmission through the specimen, the diameters of both the incident and transmission bars were standardized at 50 mm, aligning with the specimen's end diameters. Five observation points, labeled A to E, were strategically positioned on the incident and transmission bars to monitor dynamic stress wave behavior. Additionally, to enhance stress wave transfer and reduce experimental discrepancies, the particles at the interface between the bars and the specimen were meticulously arranged, possessing a radius equivalent to the smallest particle in the specimen.

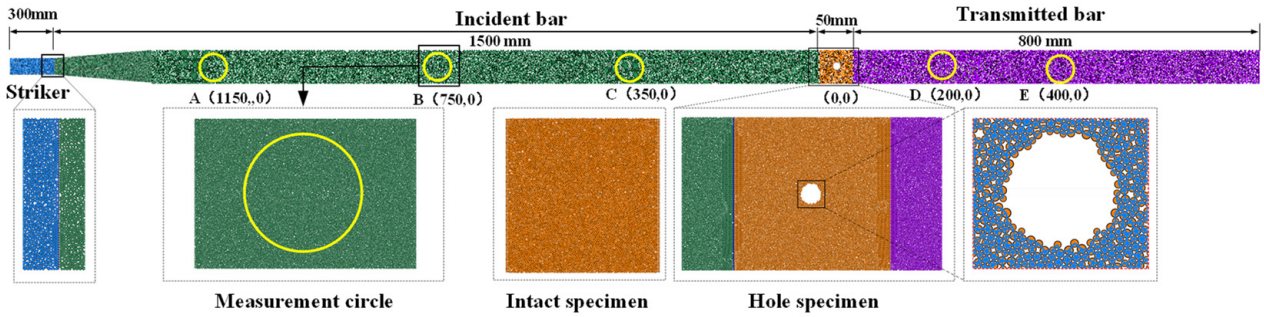

Figure 5. Schematic diagram of the SHPB numerical model.

A cylindrical rock specimen, measuring 50 mm in diameter and 50 mm in length, was fabricated with internal particles designed to be small and uniformly distributed, featuring particle sizes from 0.15 mm to 0.25 mm and a particle size ratio of 1.66. The porosity of the specimen was set at 0.15, adhering to a slenderness ratio of 1.0. The particle

deletion method facilitated the creation of voids within the model [46] for its effectiveness and rapidity, focusing on precise locations for particle elimination. While this approach primarily removes particles from the center of the designated area, leading to a relatively rough borehole surface, the markedly smaller particle sizes compared to the diameter of the holes ensured that the influence on the experimental results was negligible.

Despite previous findings suggesting that the influence of the numerical model on the specimen's mechanical behavior is minimal in experiments when the smallest dimension of the model is at least five times greater than the average particle diameter, with a minimum of five particles spanning the end faces [47–49], the authors of this study chose to utilize smaller particles to increase experimental precision. This strategy guaranteed that both the smallest dimension of the specimen and the average particle size were adequately large, facilitating a more accurate depiction of the model's mechanical damage features from a macroscopic perspective throughout the loading phase. As a result, the impact of particle size on the simulation's outcomes was minimized, enhancing the accuracy of the experimental findings.

2.4. Experimental and Simulation Results Validation and Micro-Parameter Verification

In numerical simulation experiments, micro-parameters, such as particles and bonding keys, are crucial in determining the model's macroscopic mechanical properties. Calibrating its micro-parameters becomes essential to ensure congruence between the numerical model and empirical experiments. Despite the lack of a direct quantitative correlation between micro-parameters and macroscopic mechanical properties, calibration is achieved through iterative experimentation until the simulation results mirror those from controlled laboratory experiments. Table 1 presents the microscopic parameters of the calibrated model. In practical experiments, particularly those involving stress wave propagation through a Hopkinson pressure bar, the bar remains elastic without undergoing fracture. This necessitates assigning exceptionally high mesoscopic bond strengths to simulate real-world conditions accurately.

Table 1. Microscopic parameters of the numerical model.

Macroscopic Parameter		Specimen	SHPB Bar
Particle	Radius (mm)	0.3~0.5	0.3~0.9
	Density (kg/m^3)	2570	7800
	Elastic modulus (GPa)	8.7	210
	Stiffness ratio k_n/k_s	2.0	2.0
	Friction coefficient	0.5	0.5
Bond	Effective modulus (GPa)	8.7	210
	Stiffness ratio k_n/k_s	2.0	2.0
	Tensile strength (MPa)	50	1×10^{100}
	Shear strength (MPa)	50	1×10^{100}

By comparing the dynamic stress–strain curves obtained from controlled laboratory experiments with those generated by numerical simulations, as shown in Figure 6, the alignment between the curves of the experimental specimens and the numerical model under the same loading conditions is strikingly high. Moreover, the patterns of degradation and failure exhibited in the numerical simulations closely reflect those observed in laboratory experiments. These comparisons confirm the accuracy of the Discrete Element Method (DEM) model, showcasing the ability of the developed numerical model to accurately reproduce the dynamic mechanical behaviors and failure mechanisms witnessed in specimens undergoing dynamic impact tests.

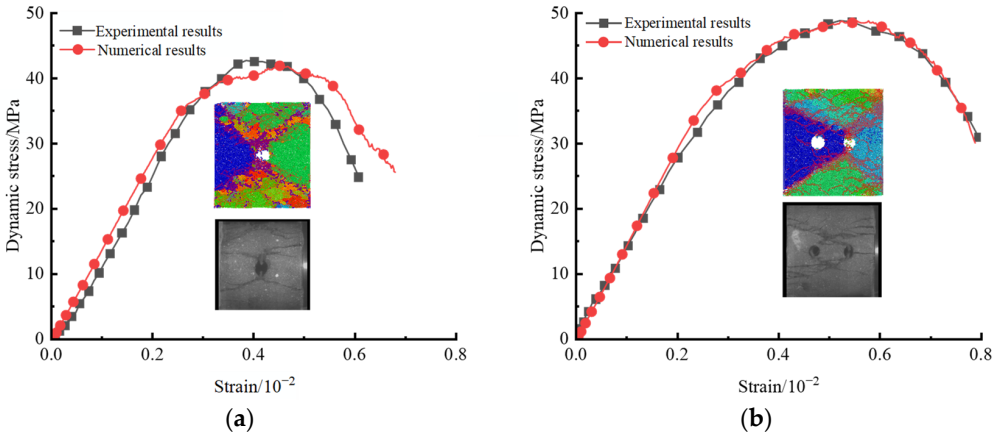

Figure 6. Comparison of dynamic stress–strain curves and failure modes between experimental and numerical results: (**a**) single 8 mm hole specimen under a strain rate condition of 100 s^{-1}; (**b**) double 6 mm hole specimens under a strain rate condition of 200 s^{-1}.

3. Validation of Experimental Results and Reliability of the Numerical Model

3.1. Propagation of Dynamic Stress Waves

In Split Hopkinson Pressure Bar (SHPB) experiments, the non-uniform propagation of dynamic stress waves can affect the precision of experimental outcomes. Thus, assessing the dispersion effect of dynamic stress waves becomes crucial. To verify whether the SHPB model system aligns with the assumption of one-dimensional stress wave propagation, an examination of the stress wave distribution at designated measurement points within the DEM model is imperative. As a result, an evaluation of the SHPB system's adherence to theoretical assumptions was carried out.

Five measurement circles, A to E, were positioned within the model bars. Circles A, B, and C recorded the incident (ε_i) and reflected (ε_r) stress wave data in the incident bar, while circles D and E registered the transmitted stress wave (ε_t) data in the transmission bar. Figure 7a,b illustrate both bars' axial and radial time–stress curves. Figure 7a shows that the peak stresses of the axial curves for both the incident and transmitted stress waves closely match, indicating minimal propagation attenuation. The radial stress curves also display sawtooth fluctuations, with peak stresses considerably lower than the axial stresses, thus not affecting the experimental results. This analysis of stress waves proves that the SHPB numerical model conforms to the one-dimensional stress wave assumption, confirming its precision.

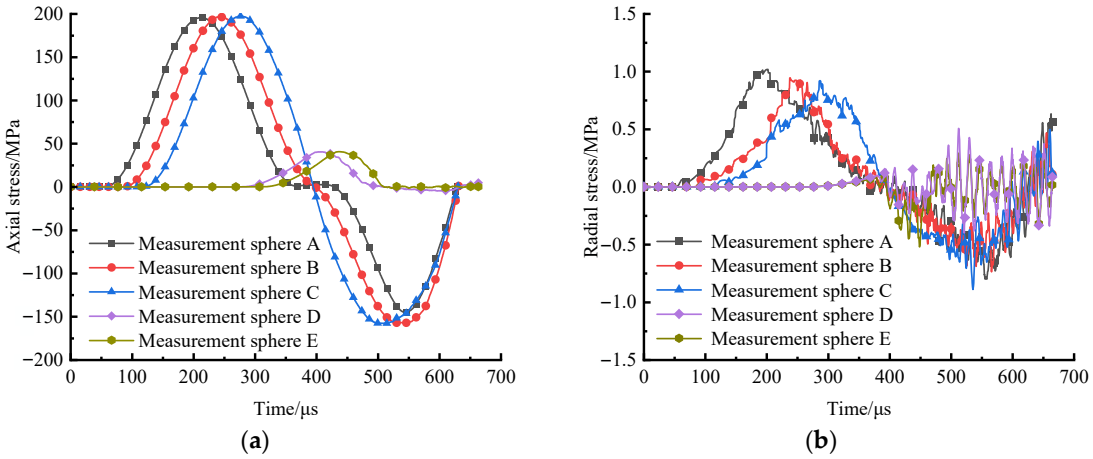

Figure 7. Stress histories monitored by measuring spheres (A–E) in the simulation experiment (loading strain rate of 200 s^{-1}): (**a**) axial stress; (**b**) radial stress.

3.2. Verification of Dynamic Stress Equilibrium

To ensure the validity of the data derived from Split Hopkinson Pressure Bar (SHPB) simulation experiments, verifying the dynamic equilibrium of the rock specimen under axial impact is essential. During the axial impact loading, the stress history documented at both ends of the specimen should demonstrate a high degree of uniformity. A direct measurement strategy is utilized to monitor the stress history at the interfaces between the bars and the specimen. The equilibrium of stress at the specimen's ends is determined using the force balance coefficient, computed by the following formula:

$$\mu = 2(F_{In} - F_{Tr})/(F_{In} + F_{Tr}) \quad (4)$$

Previous sections contrasted stress–strain curves and failure mechanisms from laboratory and numerical simulation experiments, validating the accuracy of the numerical model's outcomes. To highlight different stages of the specimen's failure process, this experiment segmented the stress–damage time curve of the rock specimen and selected specimens of notable significance for illustration, as shown in Figure 8.

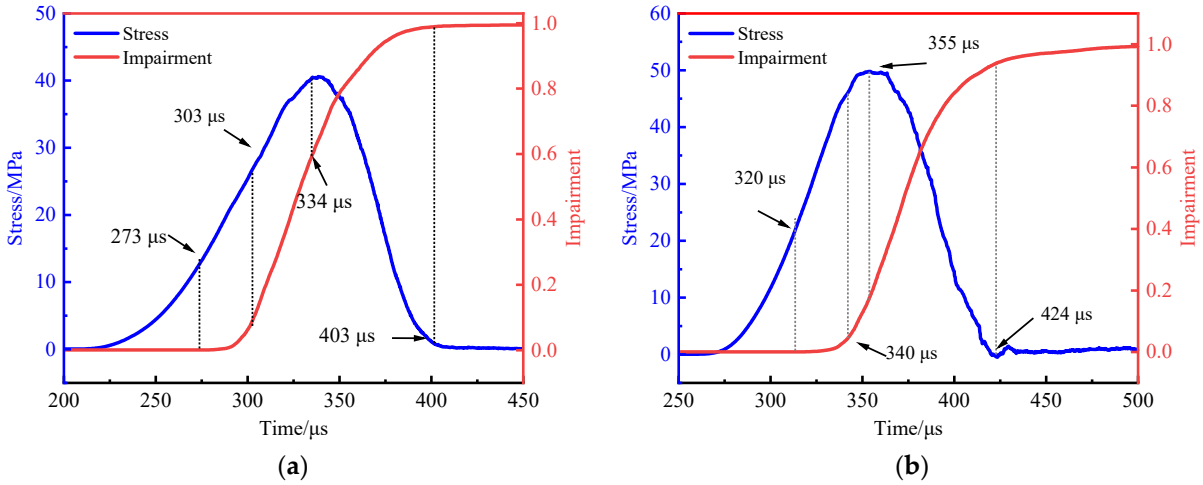

Figure 8. Stress–damage time curves (**a**) for an 8 mm hole specimen; (**b**) for a double 6 mm hole specimen.

The stress–damage time curve shown in Figure 8 highlights four crucial phases: degradation onset, yield point, peak stress, and complete failure. The degradation onset indicates the initial crack formation, whereas the yield point represents a marked acceleration in crack propagation. As their designations suggest, peak stress refers to the highest stress level experienced by the specimen, and complete failure marks the point at which the specimen fails entirely.

Generally, the stress history data recorded at the incident end face of the specimen should align closely with those from the transmission end face. A discrepancy of less than 10% from a defined critical value falls within acceptable precision limits for numerical experiments. Figure 9 illustrates the time–stress curves at the specimen's end faces, and examination of these curves reveals a tight concordance between the stress profiles at both specimen ends. The calculation of the stress balance coefficient shows that the variation in stress at the specimen ends consistently stays below 10% between T_d and T_w. This compliance with the dynamic equilibrium standards validates the dependability of the data from the dynamic numerical experiment.

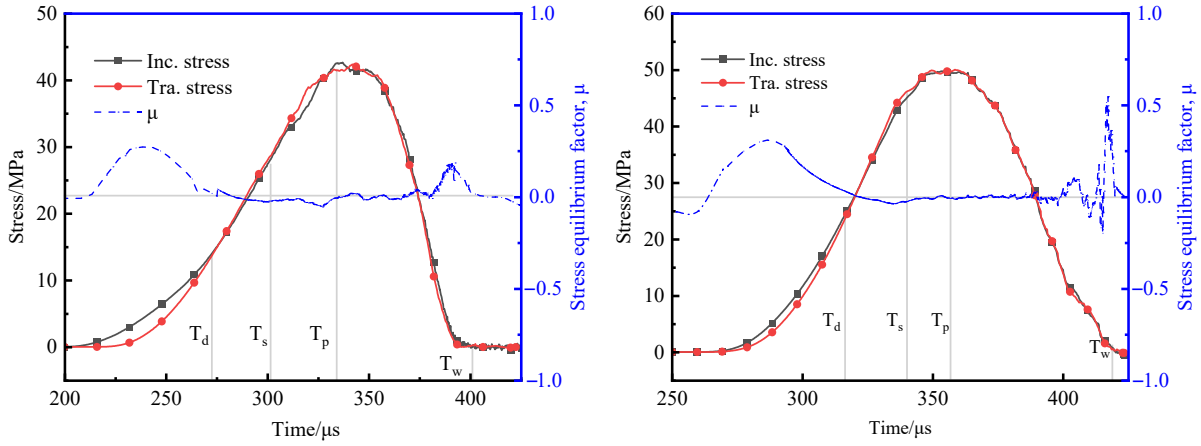

Figure 9. Dynamic stress equilibrium check: (**a**) single 8 mm hole specimen; (**b**) double 6 mm hole specimen.

4. Simulation Results and Analysis

4.1. Simulation Scheme and Stress–Strain Curves

Numerical simulation experiments, drawing inspiration from laboratory experiments, were conducted. Due to the limitations in specimen size, boreholes were strategically placed at the axial and radial center for specimens with a single borehole, and at the points where the radial vertices intersect with the axial trisection for specimens with two boreholes. The specimens were subjected to similar strain rates during the impact process through adjustments in the dynamic stress wave parameters. Information regarding the specific loading schemes employed in the experiments is detailed in Table 2.

Table 2. Numerical simulation experiment scheme.

Experimental Equipment	Drilling Parameters (Diameter/mm)		Strain Rate (s^{-1})
	Single-Hole	Double-Hole	
Numerical Simulation of SHPB Equipment	2 mm	2 mm	60–200 s^{-1}
	4 mm	4 mm	
	6 mm	6 mm	
	8 mm	8 mm	

Figures 10 and 11 illustrate the stress–strain curves for various specimens subjected to five analogous strain rate loading conditions. Although peak stress values differ, the general patterns of the curves remain uniform. Starting from the curve's origin, the stress–strain relationship initially exhibits a linear escalation. However, approaching peak stress, the rate of escalation moderates; strain continues to ascend while stress accumulation slows. Prior studies identify the stress magnitude at the maximum load point as the dynamic peak stress, denoting the specimen's dynamic mechanical prowess. The strain at this juncture, known as the dynamic peak strain, reflects the maximum distortion the specimen can endure before succumbing to failure. After surpassing peak stress, as damage within the specimen intensifies, its ability to serve as a unified medium for stress transmission weakens, resulting in a decrease in the amount of stress capable of being borne and thus marking the transition into the unloading phase.

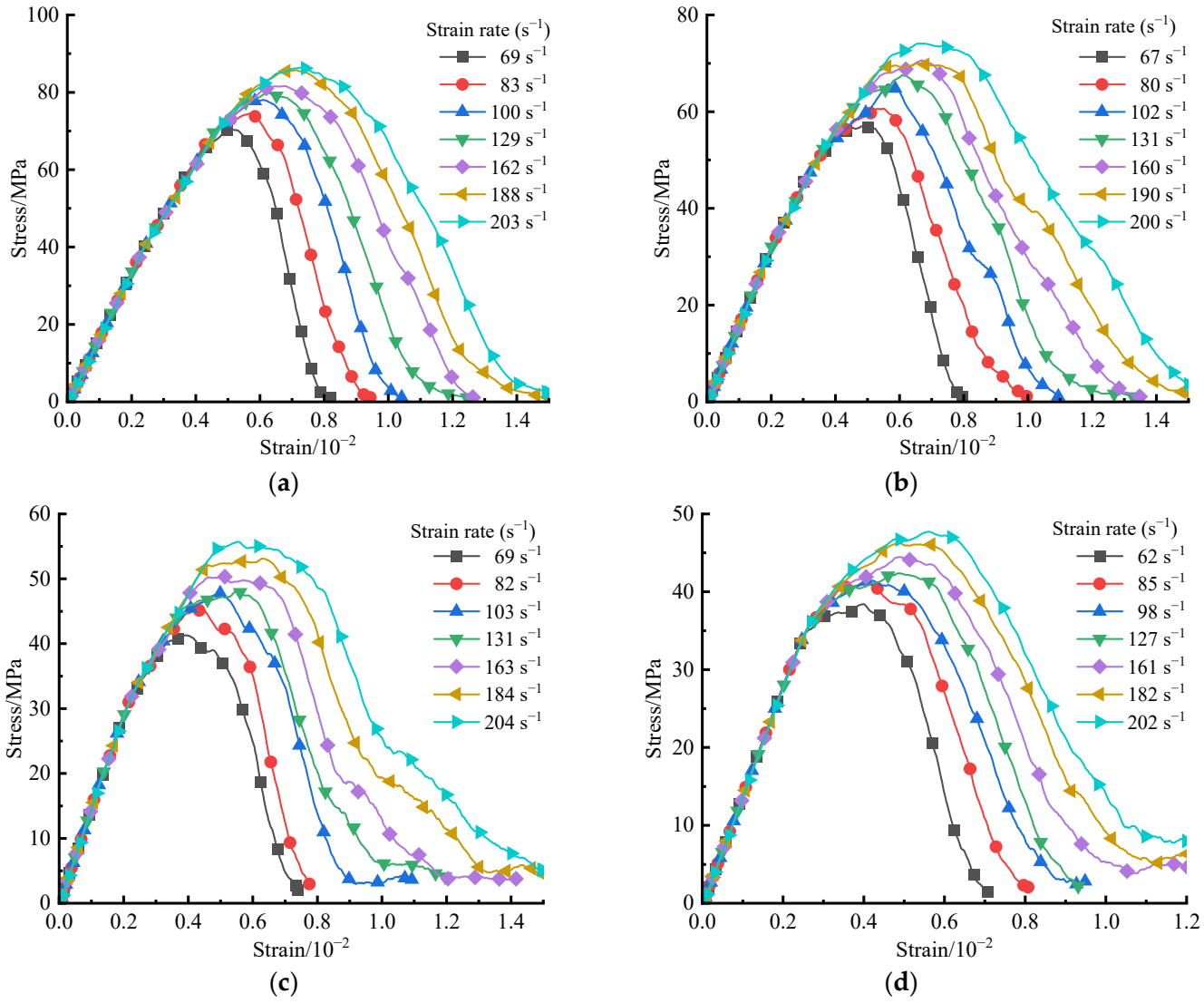

Figure 10. Dynamic stress–strain curves of single-hole specimens at different strain rates: (**a**) 2 mm hole specimen; (**b**) 4 mm hole specimen; (**c**) 6 mm hole specimen; (**d**) 8 mm hole specimen.

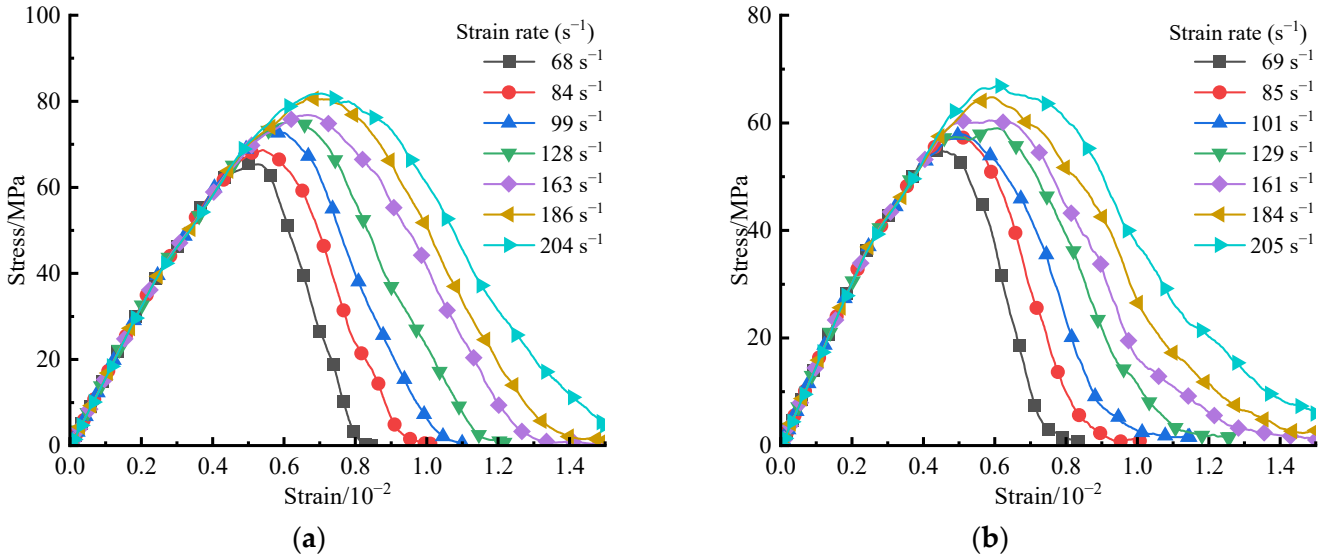

Figure 11. *Cont.*

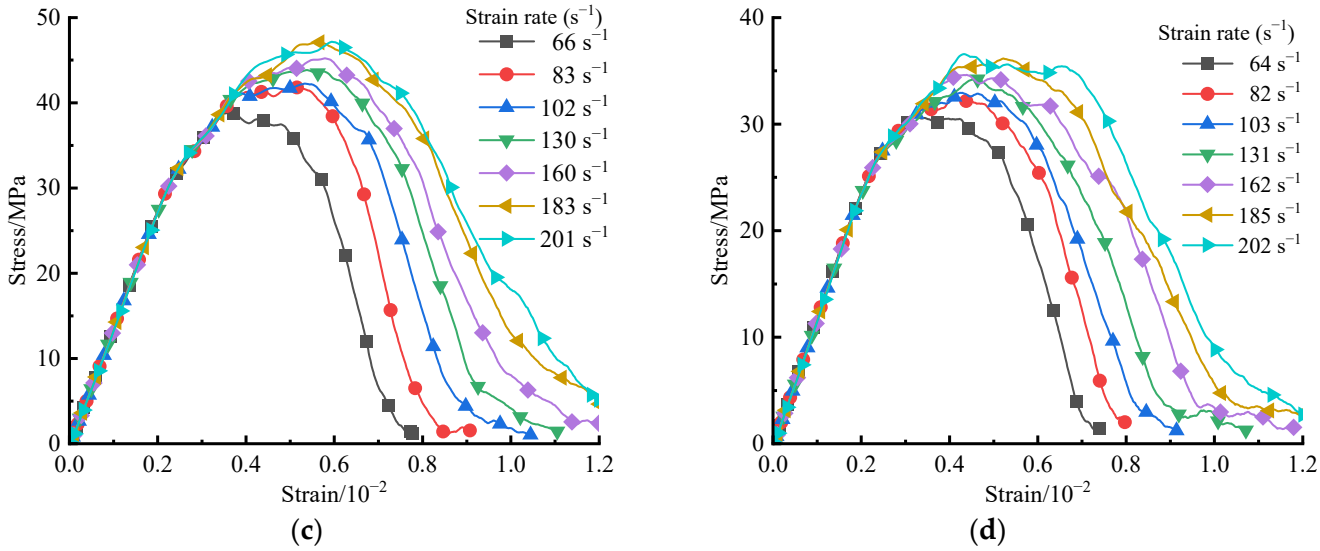

Figure 11. Dynamic stress–strain curves of double-hole specimens at different strain rates: (**a**) 2 mm hole specimen; (**b**) 4 mm hole specimen; (**c**) 6 mm hole specimen; (**d**) 8 mm hole specimen.

4.2. The Impact of Strain Rate on the Dynamic Mechanical Parameters of Rock Specimens

To investigate how holes affect the dynamic mechanical properties of rocks under different strain rate conditions, data on dynamic mechanical strength and peak strain for specimens under various loading scenarios were compiled, as shown in Figures 12 and 13. The analysis of Figure 12 indicates that the correlation between the diameter of the specimen holes and their dynamic mechanical strength approximates a linear relationship, conforming closely to the linear equation (Y = a + bx). Furthermore, the dynamic mechanical strength and peak strain for all specimens in this study were observed to increase with strain rate, consistent with previous research findings. However, the sensitivity of both dynamic mechanical strength and peak strain in specimens with two holes to changes in strain rate decreases as the hole diameter increases, leading to less marked variations in dynamic mechanical strength and peak strain under different strain rate conditions. This effect becomes more pronounced with the enlargement of hole sizes.

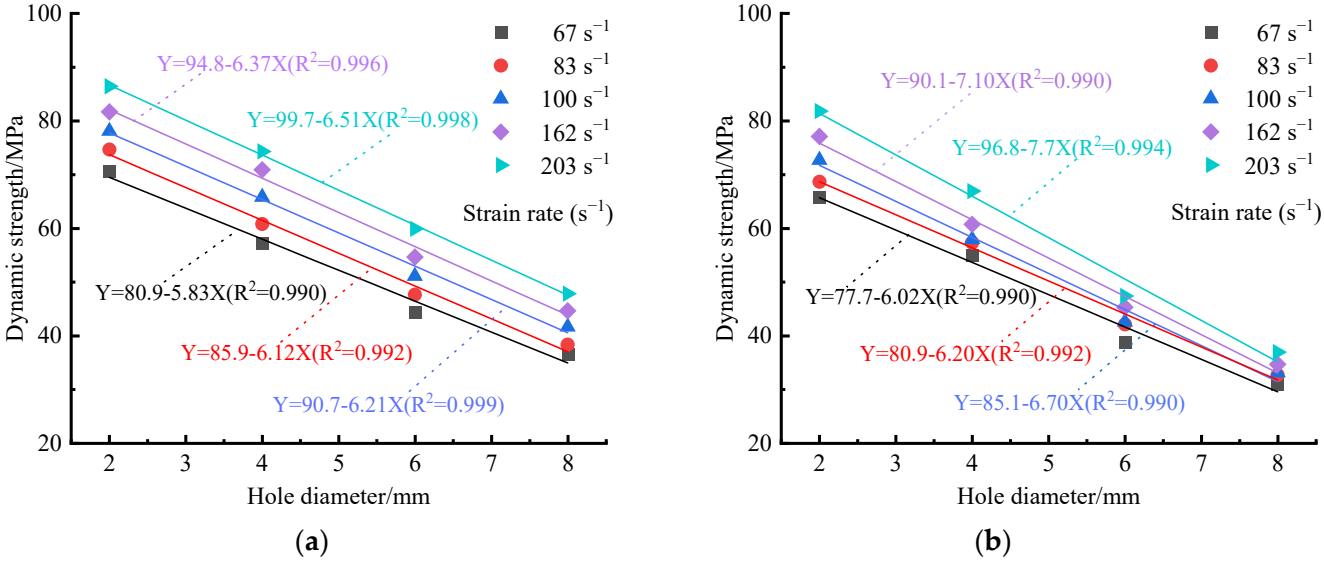

Figure 12. Influence of strain rate and hole diameter on the dynamic mechanical strength of rock specimens: (**a**) single-hole specimen; (**b**) double-hole specimen.

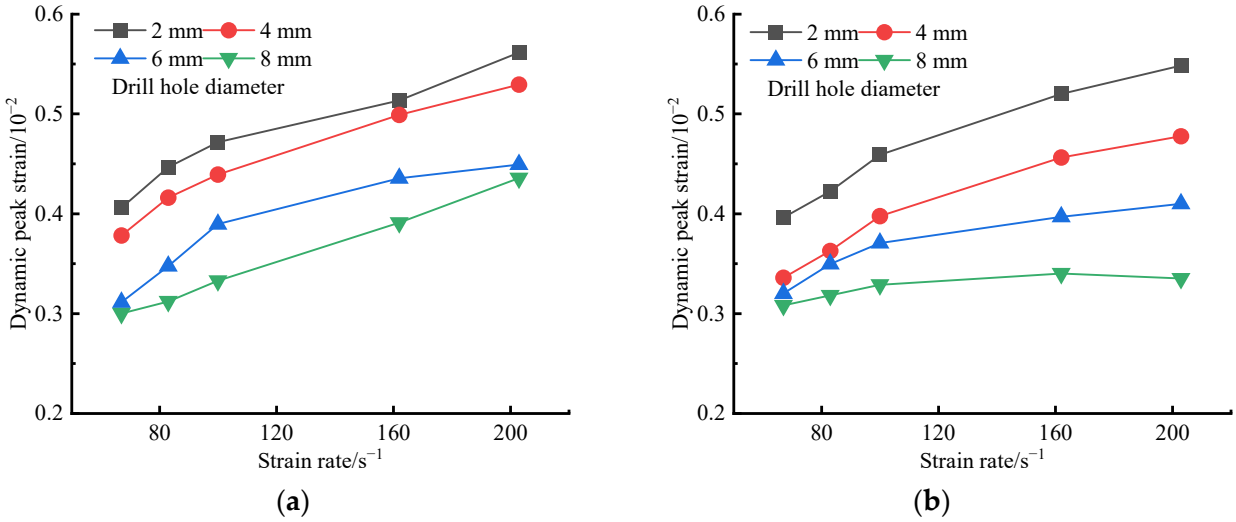

Figure 13. Influence of strain rate and hole diameter on the peak strain of rock specimens: (**a**) single-hole specimen; (**b**) double-hole specimen.

Previous studies indicate that the dynamic mechanical behavior of specimens with two holes is less affected by strain rates, though the precise mechanical explanations for this phenomenon remain elusive. However, certain investigations have pinpointed the critical role of the internal stress field's evolution under external forces in causing rock material failure. This research studies the evolution law of the stress field of test specimens with holes using a numerical model. For the single-hole specimen, concentric measurement circles with a radius of 2 mm were methodically positioned at 30° intervals around the hole's center, extending outward to a 6 mm radius, thus forming circular measurement zones. Conversely, in the case of double-hole specimens, an elliptical configuration for the stress field measurements was utilized, with uniform parameters set for tracking angles and radial distances.

Figure 14a depicts the vertical stress field distribution around the borehole of a specimen with a single 6 mm hole, where the impact load direction is parallel to the X-axis. This orientation results in the highest stress concentrations at 90° and 270° from the borehole center, and the lowest stress at 0° and 180°. Near the borehole's apex and parallel to the loading direction, the stress levels are low, while regions perpendicular to the load direction at the hole's apex register high stress. Drilling leads to a stress redistribution in the rock, causing stress to intensify from the borehole's apex in the X-direction towards the apex in the Y-direction. An increase in strain rate is associated with a rise in vertical stress intensity across various angles. In contrast, Figure 14b demonstrates that the stress at 0° and 180° remains minimal for a specimen with two holes, with a more uniform vertical stress distribution observed at other angles. With an escalation in strain rate, the vertical stress intensity at various angles tends to stabilize, indicating that under high strain rate conditions, the stress distribution in specimens with two holes becomes more uniform, devoid of significant stress concentrations.

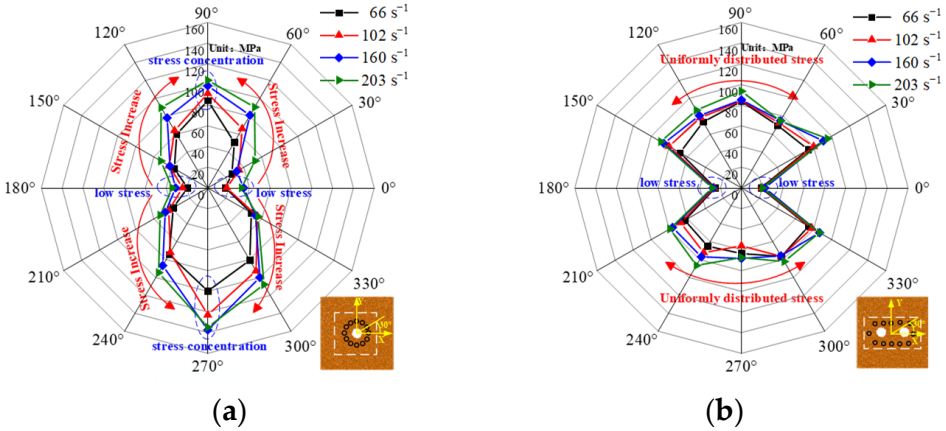

Figure 14. Vertical stress distribution in specimens under different strain rate loading conditions: (**a**) single-hole rock specimens; (**b**) double-hole rock specimens.

4.3. Failure Behaviours of Specimens with Holes

After the experiments, the failure modes of specimens with holes under different strain rate conditions showed consistent characteristics. To understand the differences in failure modes between single-hole and double-hole rock specimens, two specific experimental configurations (6 mm hole, 2 × 6 mm holes) were selected for an in-depth analysis of the rocks' evolving failure modes. Tables 3 and 4 (a–c) depict the patterns of fractures, failure morphology, and force chain distribution for both hole configurations under the same impact scenarios. In these illustrations, green represents tensile stress, blue signifies compressive stress, and the thickness of the force chain indicates the magnitude of internal force within the specimen. Section 3.2 elaborates on confirming the dynamic equilibrium of the SHPB model, identifying four critical time points on the stress–damage time curve to mark different stages from the onset of loading to the complete breakdown of the specimens, focusing on conditions at points T_D, T_S, T_P, and T_W. Tables 3 and 4 (d) also present the failure modes observed in laboratory experiments, which were subsequently compared and validated against the numerical model's degradation patterns.

Table 3. Progressive failure modes of single-hole specimens: (a) crack distribution; (b) fragmentation distribution; (c) force chain pattern; (d) laboratory experiment image.

	T_d	T_s	T_p	T_w
(a)	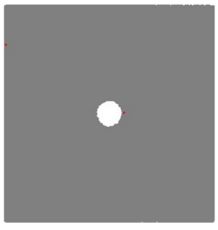	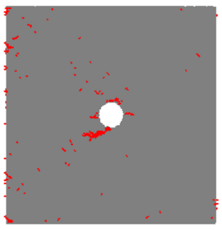	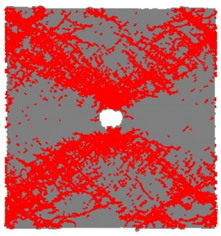	
(b)	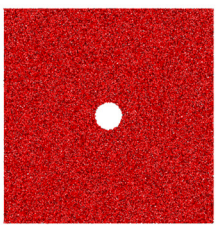	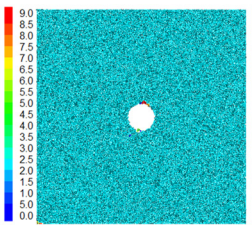	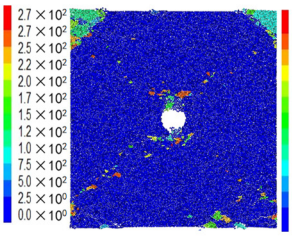	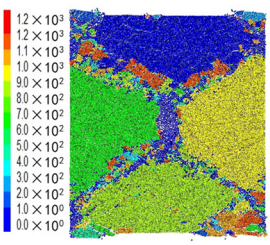

Table 3. *Cont.*

	T_d	T_s	T_p	T_w
(c)	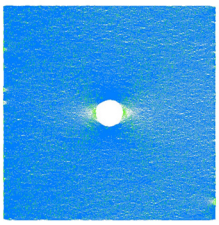	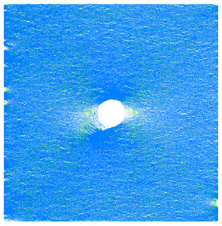	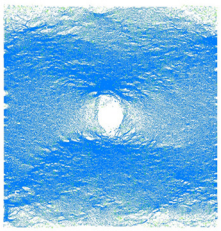	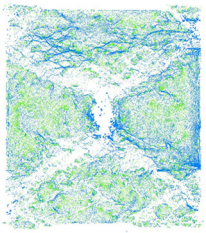
(d)	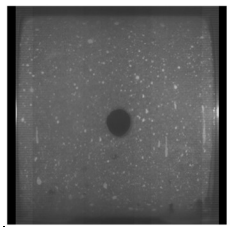	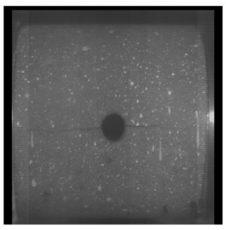	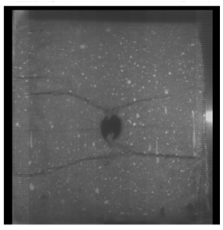	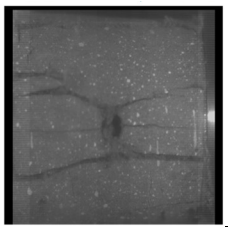

Table 4. Progressive failure modes of double-hole specimens: (a) crack distribution; (b) fragmentation distribution; (c) force chain pattern; (d) laboratory experiment image.

	T_d	T_s	T_p	T_w
(a)	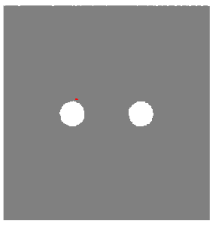	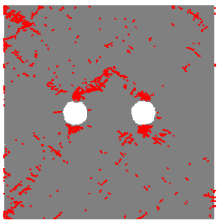		
(b)	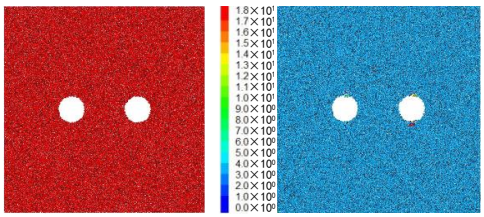	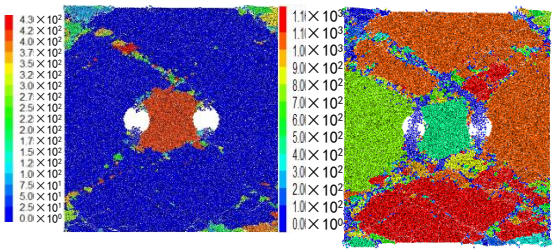		
(c)	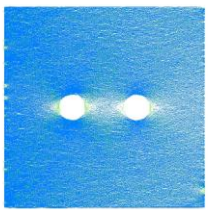	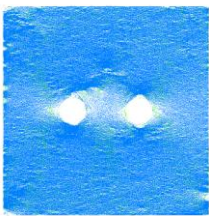	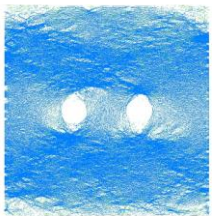	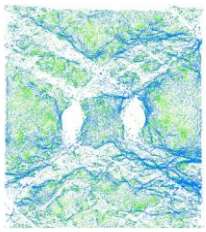
(d)	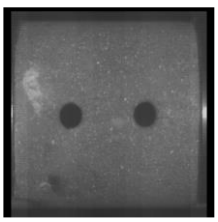	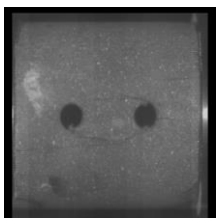	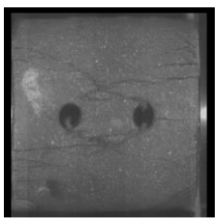	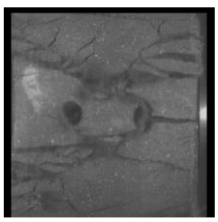

In Table 3, point T_d signifies the commencement of degradation for the single-hole specimen, highlighted by the appearance of initial microcracks, with the specimen displaying its first minor crack and minimal overall damage. The force chain distribution remains even, and tensile cracks begin to form at the hole's axial apex, following the direction of the stress wave, attributable to tensile stress. On the other hand, a concentration of compressive stress is noted at the hole's crest, perpendicular to the stress wave's direction, consistent with observations from studies on vertical stress field distribution. As the specimen is subjected to stress up to point T_s, it enters the yield phase, characterized by a notable escalation in the number of cracks, especially around the hole's axial and radial apexes. Axial compressive deformation in the specimen leads to the emergence of minor end-face cracks. The stress concentration at the hole's vertical apex shifts, with the force chain in the stressed region moving to the crack initiation area, thus aiding crack extension. Moreover, the force chain distribution begins to display irregularity, becoming more pronounced in the crack initiation zone. Upon reaching peak stress (point T_p), cracks stemming from the hole converge with end-face cracks, creating macroscopic X-shaped fractures. Nevertheless, the specimen remains in one piece. The once even force chain distribution now changes, causing detachment of debris. In regions of intersecting cracks, force chains intensify and cluster around the new cracks. Finally, at point T_w, the drilling hole is thoroughly fragmented and deformed, with macroscopic X-shaped cracks fully matured, segmenting the specimen into four separate sections. Consequently, force chains are now concentrated within these four large fragments, signifying the specimen's inability to sustain load.

In Table 4, point T_d marks the initial phase for the double-hole specimen, where the ends reach dynamic stress equilibrium with no evident damage. The force chain pattern around the holes resembles that seen in single-hole specimens, but a marked difference is the sparser density of contact force chains in the rock bridge area between the two holes. Upon loading the specimen to point T_s, it enters the yield phase. Under tensile stress, minor cracks start from the axial apex of each hole, running parallel to the stress wave direction. Concurrently, cracks from the radial apex extend towards the center's rock bridge area, effectively beginning to segment this bridge into separate blocks. This leads to a distribution of force chains that reflects the emerging crack patterns. At point T_p, peak stress is reached at the specimen's end faces, causing rapid crack propagation, while the initial axial tensile cracks halt their advance. Cracks around the rock bridge and those on the end faces merge, forming a significant X-shaped fracture centered on the rock bridge. An analysis of the specimen's fractured state shows the rock bridge divided into blocks by these cracks, with the specimen's edges also showing signs of fracture, indicating a tendency for the segmented blocks to separate. Force chains are now primarily concentrated around the major macroscopic fractures. The specimen is completely fragmented in the post-peak stress phase (point T_w), with its overall damage reaching a maximum. The resulting debris forms five separate sections, characterized by a pronounced X-shaped fracture originating from the rock bridge. Force chains are restricted to the larger fragments, indicating the specimen's inability to bear loads evenly.

4.4. Final Failure Modes

Tables 5 and 6 show the displacement field and crack distribution diagrams for various specimens after undergoing uniaxial dynamic impact. In the displacement fields, different colors represent distinct levels of relative displacement, facilitating the visualization of movement within the specimen. Likewise, in the crack distribution diagrams, unique colors indicate the types of cracks present: green illustrates tensile cracks, and blue highlights shear cracks. The predominant cause of failure in the specimens was the advancement of edge cracks within the conical blocks situated at the ends of the specimens, reflecting the critical points of stress concentration and fracture initiation.

Table 5. Displacement field and crack distribution of single-hole specimen failure modes.

Diameter of Hole	Strain Rate (100 s^{-1})		Strain Rate (200 s^{-1})	
	Displacement Field	Crack Distribution	Displacement Field	Crack Distribution
2 mm	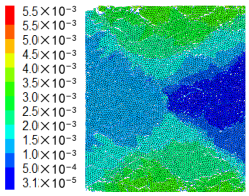	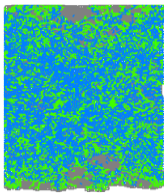	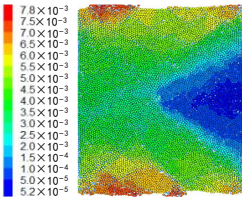	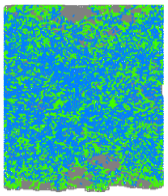
4 mm	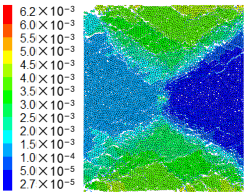	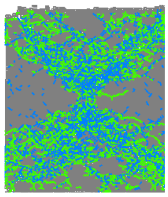	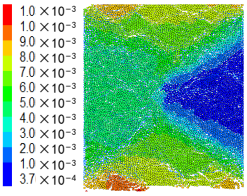	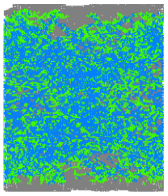
6 mm	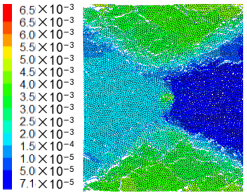	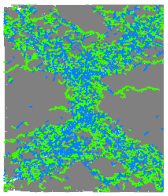	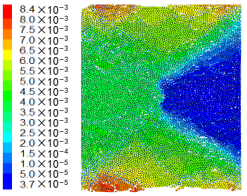	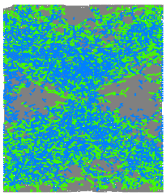
8 mm	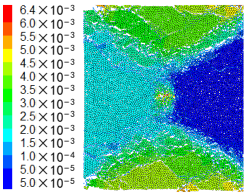	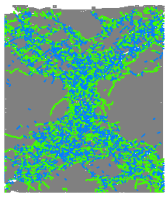	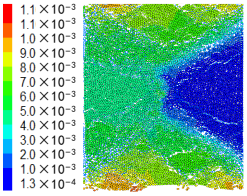	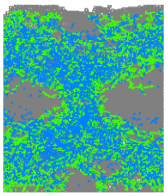

The comparative analysis shown in Table 5, focusing on the failure modes of specimens with holes subjected to the same strain rate loading conditions, reveals that a larger hole diameter leads to an increased relative displacement of blocks at the specimen's incident face and a denser concentration of cracks surrounding the macro X-shaped main crack. This effect is likely due to the larger holes providing more room for the movement of conical blocks, which in turn promotes the formation of macrocracks.

In the simulated impact experiments that were conducted, the occurrence of tensile and shear cracks was meticulously recorded across various failure modes in the specimens. To better visualize the variation in the number of cracks, the specimen with the smallest number of cracks under a strain rate of 100 s^{-1} and with an 8 mm hole, which exhibited 2600 shear cracks, was chosen as a baseline for comparison. Figure 15 reveals that an increase in hole diameter is associated with a reduction in both tensile and shear crack numbers. This reduction is attributed to the holes facilitating the displacement of conical blocks, which in turn lessens microcrack generation. Consequently, this indicates that larger hole diameters encourage the formation of significant macroscopic cracks, altering the overall failure dynamics of the specimens.

Table 6. Displacement field and crack distribution of double-hole specimen failure modes.

Diameter of Hole	Strain Rate (100 s^{-1})		Strain Rate (200 s^{-1})	
	Displacement Field	Crack Distribution	Displacement Field	Crack Distribution
2 mm	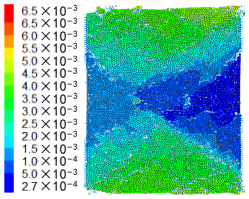	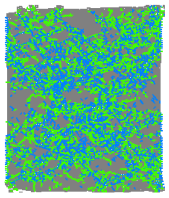	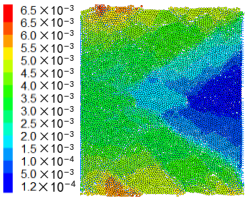	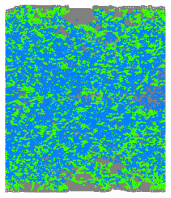
4 mm	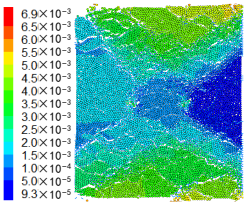	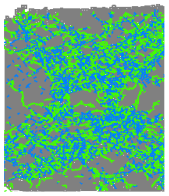	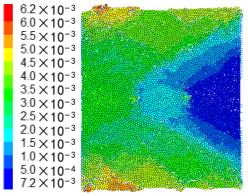	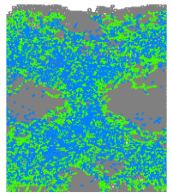
6 mm	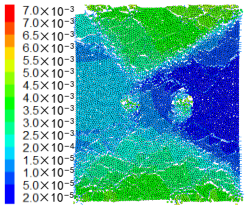	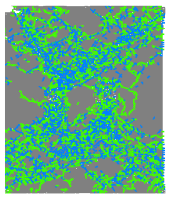	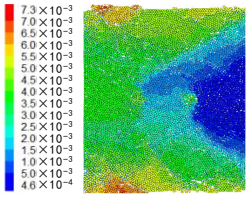	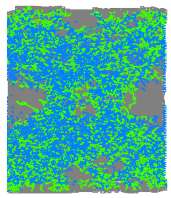
8 mm	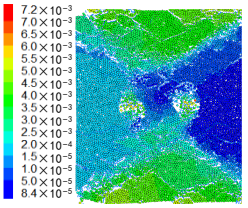	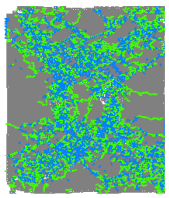	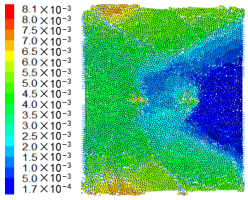	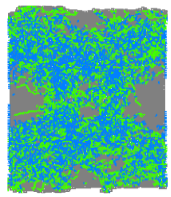

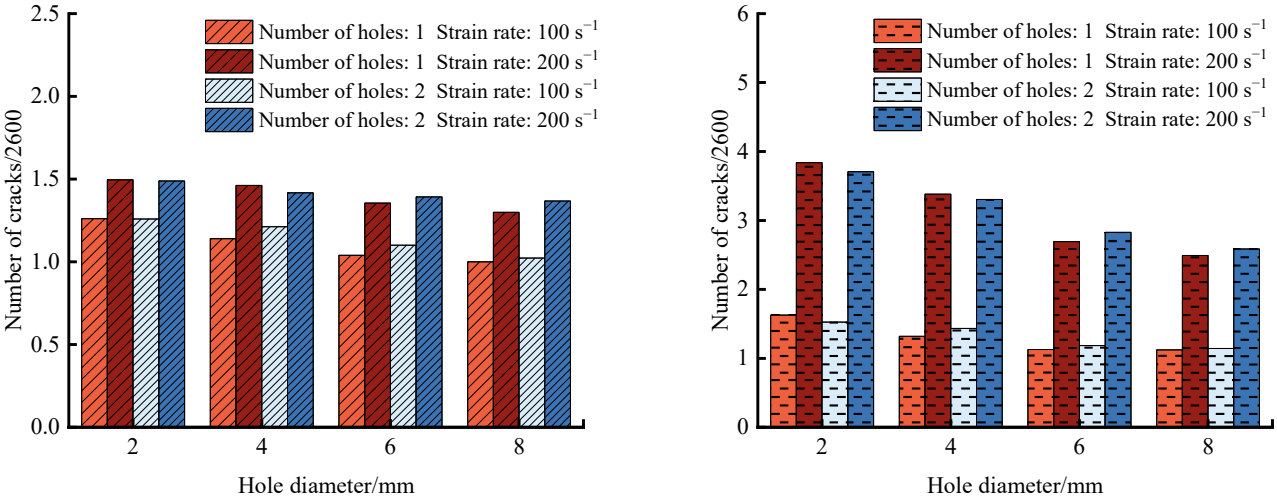

Figure 15. Comparison of cracks in specimens with holes at different strain rates: (**a**) tensile cracks; (**b**) shear cracks.

In dynamic impact experiments, strain rate emerges as a crucial determinant of specimen mechanical behavior. Comparative analysis of displacement field diagrams at strain rates of 200 s^{-1} and 100 s^{-1} reveals that displacement at the conical blocks on the incident

end is markedly greater under higher strain rate conditions, accompanied by pronounced block peeling at the specimen edges. As illustrated in Figure 16, high strain rates lead to a substantial increase in shear crack quantity, suggesting that specimen failure modes at elevated strain rates are predominantly governed by shear cracks, resulting in increased fragmentation.

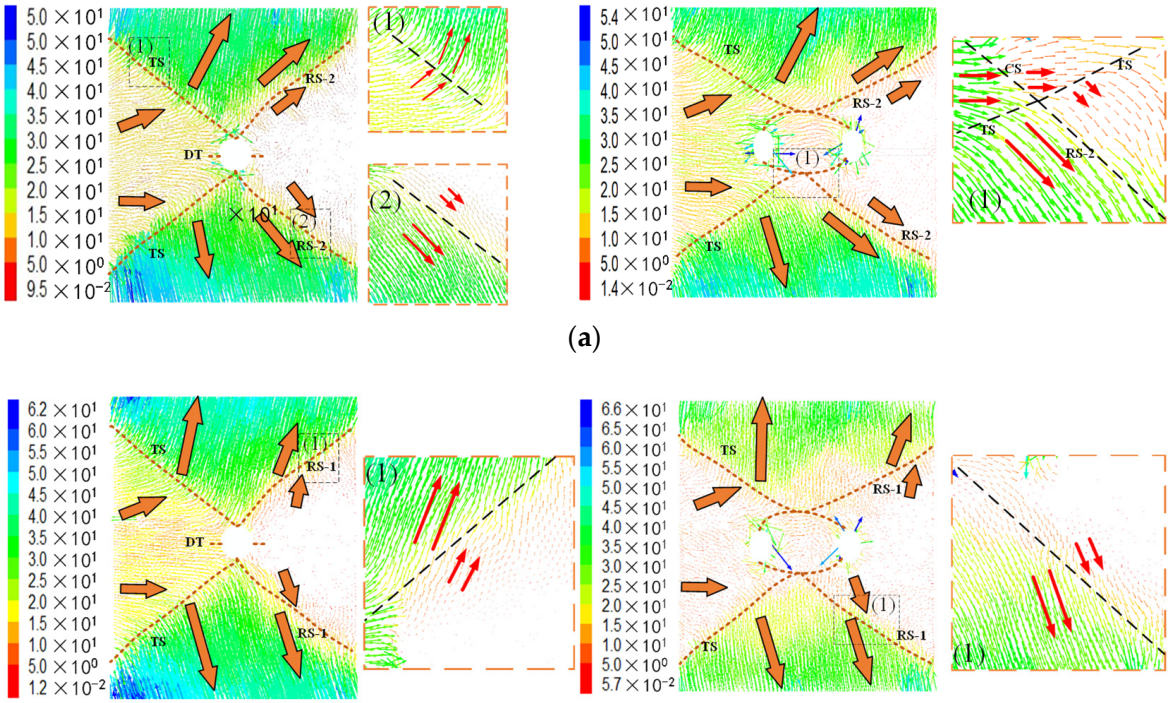

Figure 16. Displacement field diagram of specimens with holes at the time of ultimate failure: (**a**) loading condition at a strain rate of 100 s^{-1}; (**b**) loading condition at a strain rate of 200 s^{-1}.

5. Discussion

While prior studies have detailed the progressive failure modes of specimens with varying hole parameters, including diagrams of crack development, compressive failure morphology, and force chain patterns, they have not elucidated the cracking mechanism of macroscopic fractures during specimen degradation. Traditionally, Computed Tomography (CT) and Scanning Electron Microscopy (SEM) have been the primary methods for investigating fracture mechanisms in physical experiments, yet their high costs have limited their frequent use. Conversely, numerical simulation experiments offer a cost-effective alternative for analyzing the cracking mechanisms of macroscopic fractures. Through visual analysis of the displacement field during the loading process, these simulations can yield insights comparable to those provided by CT and SEM, but at a lower cost.

Building on the research by Chen et al. [50], the displacement field (DTL) method elucidates the fracture cracking mechanism. This technique involves segregating the displacement field into two vectors based on their orientation—either perpendicular or parallel to the fracture—and then assessing the displacement line components on either side of the fracture. For clarity, Figure 16 illustrates various vector diagrams of displacement that correspond to the rock mass's movement patterns at the fracture's extremities. These patterns are categorized into several types [30,35]: DT (Direct Tensile Fracture), RT (Relative Tensile Fracture), RS (Relative Shear Fracture), TS (Tensile Shear Fracture), and CS (Compressive Shear Fracture).

Using the displacement vector diagram of a specimen with a 6 mm hole as an illustrative example, Figure 16a,b display the displacement vector diagrams at the failure threshold under loading conditions with strain rates of 100 s^{-1} and 200 s^{-1}, respectively.

The arrows' color and length signify the displacement magnitude, whereas colors represent the displacement. Dashed lines within the diagrams delineate macroscopic fractures, and the direction and magnitude of displacement of rock model particles adjacent to the fracture are depicted through arrows, aligning with the trend of the displacement lines.

The experimental findings indicate that at the failure threshold, the principal macroscopic fractures in all specimens consist of a combination of TS (Tensile Shear Fracture) and RS (Relative Shear Fracture) cracks at the microscopic level. Specifically, the primary fractures at the specimen's incident end are identified as TS fractures, whereas those at the transmission bar end are categorized as RS fractures. During axial compressive deformation of the rock mass, variations in deformation speed and direction at the edge of the terminal conical block lead to fracture formation due to the relative movement on either side of the rock mass. While all specimens display similar macroscopic fracture patterns, microscopic fracture mechanisms exhibit variations under different strain rates, evidenced by RS-2 and RS-1 types of fractures at the transmission end under strain rates of 100 s^{-1} and 200 s^{-1}, respectively. Despite these differences, the X-shaped failure in specimens with holes under high strain rates is predominantly attributed to shear fractures, with both RS and TS fractures demonstrating shear failure characteristics at the macroscopic level. It is also noteworthy that fractures dividing the rock bridge into separate blocks at the failure threshold in double-hole specimens are primarily CS (Compressive Shear Fracture) and TS fractures. Additionally, initial tensile fractures at the axial vertices of the holes, aligned with the loading direction, do not propagate during subsequent loading phases, with shear fractures continuing to dominate the fracture expansion process.

6. Conclusions

Based on the experimental and numerical model, this study explored the impact of strain rate on the dynamic mechanical characteristics of specimens with holes. Continuous monitoring of the stress field surrounding the holes and a comparative analysis of degradation modes facilitated a comprehensive examination of the variations in stress field distribution and failure mechanisms between specimens with a single hole and those with double holes. The following conclusions can be drawn from this study:

1. All specimens demonstrated a distinct strain rate dependency, yet the sensitivity of the dynamic mechanical properties of double-hole specimens to strain rate diminished with increasing hole radius. As the strain rate escalated, the growth in dynamic mechanical strength and peak strain for double-hole specimens with larger diameters became less pronounced.
2. Upon analyzing the stress field monitoring results for each specimen under varied strain rate loading conditions, a shared trait among all specimens was identified: the emergence of low-stress zones at the axial vertices of the holes, aligned parallel to the loading direction. A key distinction was observed in the stress distribution patterns: single-hole specimens exhibited stress concentration at the radial vertices of the holes, oriented perpendicular to the loading direction. In contrast, double-hole specimens demonstrated a more uniform stress distribution across various angles, lacking distinct stress concentration zones within the strain field.
3. Under varying strain rate loading conditions, the failure patterns observed in all single-hole specimens were consistent, and double-hole specimens exhibited comparable traits. Analysis of these failure modes through displacement fields revealed that shear cracks were the primary macrocracks, which segmented the specimens into multiple blocks. While initial crack formation in both specimen types began at the specimen ends, crack initiation and propagation in single-hole specimens predominantly occurred around the holes. Conversely, in double-hole specimens, some cracks developed around the rock bridge connecting the two holes.
4. The implementation of large-diameter borehole pressure relief measures has been shown to not only enhance the stress distribution surrounding the boreholes but also facilitate the formation of macrocracks by offering displacement space for the

movement of end blocks, thereby diminishing the generation of microcracks during the failure process. Furthermore, this study revealed that under high strain rate conditions, the damage at the incident end of the rock specimen was predominantly characterized by shear cracks, which exhibited greater displacement. These insights have the potential to significantly refine borehole pressure relief strategies in deep tunnel applications.

Author Contributions: Conceptualization, C.Z.; Methodology, M.C.; Formal analysis, C.X.; Investigation, M.C. and X.W.; Resources, C.Z.; Data curation, X.W. and H.T.; Writing—original draft, Q.L.; Funding acquisition, C.Z. All authors have read and agreed to the published version of the manuscript.

Funding: This research was supported by the National Natural Science Foundation of China (52374128, 42207201).

Institutional Review Board Statement: Not applicable.

Informed Consent Statement: Not applicable.

Data Availability Statement: The raw data supporting the conclusions of this article will be made available by the authors on request.

Conflicts of Interest: The authors declare no conflict of interest.

References

1. Farhadian, H. A new empirical chart for rockburst analysis in tunnelling: Tunnel rockburst classification (TRC). *Int. J. Min. Sci. Technol.* **2021**, *31*, 603–610. [CrossRef]
2. Wu, M.; Ye, Y.; Wang, Q.; Hu, N. Development of rockburst research: A comprehensive review. *Appl. Sci.* **2022**, *12*, 974. [CrossRef]
3. Wang, J.; Chen, G.; Xiao, Y.; Li, S. Effect of structural planes on rockburst distribution: Case study of a deep tunnel in Southwest China. *Eng. Geol.* **2021**, *292*, 106250. [CrossRef]
4. Xiao, Y.X.; Feng, X.T.; Li, S.J.; Feng, G.L. Rock mass failure mechanisms during the evolution process of rockbursts in tunnels. *Int. J. Rock Mech. Min. Sci.* **2016**, *83*, 174–181. [CrossRef]
5. Mark, C. Coal bursts in the deep longwall mines of the United States. *Int. J. Coal Sci. Technol.* **2016**, *3*, 1–9. [CrossRef]
6. Wu, J.; Zhang, X.Y.; Yu, L.Y.; Zhang, L.W. Rockburst mechanism of rock mass with structural planes in underground chamber excavation. *Eng. Fail. Anal.* **2022**, *139*, 106501. [CrossRef]
7. Zhou, H.; Meng, F.; Zhang, C.; Hu, D. Analysis of rockburst mechanisms induced by structural planes in deep tunnels. *Bull. Eng. Geol. Environ.* **2015**, *74*, 1435–1451. [CrossRef]
8. Li, D.; Wang, E.; Kong, X.; Ali, M. Mechanical behaviors and acoustic emission fractal characteristics of coal specimens with a pre-existing flaw of various inclinations under uniaxial compression. *Int. J. Rock Mech. Min. Sci.* **2019**, *116*, 38–51. [CrossRef]
9. Zhang, L.M.; Chao, W.W.; Liu, Z.Y.; Cong, Y.; Wang, Z.Q. Crack propagation characteristics during progressive failure of circular tunnels and the early warning thereof based on multi-sensor data fusion. *Geomech. Geophys. Geo-Energy Geo-Resour.* **2022**, *8*, 172. [CrossRef]
10. Cai, W.; Dou, L.; Zhang, M.; Cao, W. A fuzzy comprehensive evaluation methodology for rock burst forecasting using microseismic monitoring. *Tunn. Undergr. Space Technol.* **2018**, *80*, 232–245. [CrossRef]
11. Dexing, L.; Enyuan, W.; Xiangguo, K.; Haishan, J.; Dongming, W.; Muhammad, A. Damage precursor of construction rocks under uniaxial cyclic loading tests analyzed by acoustic emission. *Constr. Build. Mater.* **2019**, *206*, 169–178. [CrossRef]
12. Shi, Y.; Zhang, W.; Wang, Y.H. Seismic elastic RTM with vector-wavefield decomposition. *J. Geophys. Eng.* **2019**, *16*, 509–524. [CrossRef]
13. Gao, F.X.; Wang, Y.H. Radiation pattern analyses for seismic multi-parameter inversion of HTI anisotropic media. *J. Geophys. Eng.* **2020**, *17*, 65–75. [CrossRef]
14. Li, Z.L.; He, X.Q.; Dou, L.M.; Song, D.Z. Investigating the mechanism and prevention of coal mine dynamic disasters by using dynamic cyclic loading tests. *Saf. Sci.* **2019**, *115*, 215–228. [CrossRef]
15. Qiu, L.M.; Liu, Z.T.; Wang, E.Y.; He, X.Q. Early-warning of rock burst in coal mine by low-frequency electromagnetic radiation. *Eng. Geol.* **2020**, *279*, 105755. [CrossRef]
16. Zhu, W.B.; Yu, S.C.; Xu, J.M. Influence of the elastic dilatation of mining-induced unloading rock mass on the development of bed separation. *Energies* **2018**, *11*, 785. [CrossRef]
17. Yang, H.Q.; Zhang, N.; Han, C.L.; Sun, C.L. Stability control of deep coal roadway under the pressure relief effect of adjacent roadway with large deformation: A case study. *Sustainability* **2021**, *13*, 4412. [CrossRef]
18. Fu, Q.; Yang, J.; Wu, X.; Liu, Y.X. Study on the Method of Pressure Relief and Energy Absorption for Protecting Roadway Under Thick and Hard Roof. *Rock Mech. Rock Eng.* **2023**, *56*, 7177–7196. [CrossRef]

19. Wu, W.X.; Gong, F.Q. Dynamic tensile strength weakening effect of pretension stressed red sandstone under impact load. *J. Cent. South Univ.* **2023**, *30*, 3349–3360. [CrossRef]
20. Wu, W.X.; Gong, F.Q.; Jiang, Q. Influence of water on rockburst of surrounding rock in deep circular tunnels under triaxial internal unloading conditions. *Tunn. Undergr. Space Technol.* **2023**, *138*, 105165. [CrossRef]
21. Yang, S.Q.; Chen, M.; Tao, Y. Experimental study on anchorage mechanical behavior and surface cracking characteristics of a non-persistent jointed rock mass. *Rock Mech. Rock Eng.* **2021**, *54*, 1193–1221. [CrossRef]
22. Li, C.C. Principles and methods of rock support for rockburst control. *J. Rock Mech. Geotech. Eng.* **2021**, *13*, 46–59. [CrossRef]
23. Xie, S.R.; Jiang, Z.S.; Chen, D.D.; Wang, E. Failure mechanism of continuous large deformation and a novel pressure relief control technology on the two sides of deep coal roadway. *Eng. Fail. Anal.* **2023**, *144*, 106941. [CrossRef]
24. Liu, S.B.; Liu, H.F.; Li, S.G.; Shuang, H.Q. Experimental study on the effect of unloading rate on the damage of coal with boreholes. *Fuel* **2024**, *357*, 129965. [CrossRef]
25. Xie, S.R.; Jiang, Z.S.; Chen, D.D.; Wang, E. A new pressure relief technology by internal hole-making to protect roadway in two sides of deep coal roadway: A case study. *Rock Mech. Rock Eng.* **2023**, *56*, 1537–1561. [CrossRef]
26. Chen, M.; Zhang, Y.L.; Zang, C.W.; Zhang, G.C. Experimental investigation on pressure relief mechanism of specimens with prefabricated reaming boreholes. *Rock Mech. Rock Eng.* **2023**, *56*, 2949–2966. [CrossRef]
27. Lin, P.; Wong, R.H.; Tang, A. Experimental study of coalescence mechanisms and failure under uniaxial compression of granite containing multiple holes. *Int. J. Rock Mech. Min. Sci.* **2015**, *77*, 313–327. [CrossRef]
28. Li, Y.Y.; Guo, R.W.; Zhang, S.C.; Chen, B. Experimental Study on Pressure Relief Mechanism of Variable-Diameter Borehole and Energy Evolution Characteristics of the Surrounding Rock. *Energies* **2022**, *15*, 6596. [CrossRef]
29. Li, J.; Zhao, J.; Wang, H.C.; Wang, H.C. Fracturing behaviours and AE signatures of anisotropic coal in dynamic Brazilian tests. *Eng. Fract. Mech.* **2021**, *252*, 107817. [CrossRef]
30. Han, Z.Y.; Xie, S.J.; Li, D.Y. Discrete element study on the mechanical behavior of flawed rocks under dynamic compression. *Theor. Appl. Fract. Mech.* **2022**, *121*, 103516. [CrossRef]
31. Zhang, Q.B.; Zhao, J. A review of dynamic experimental techniques and mechanical behaviour of rock materials. *Rock Mech. Rock Eng.* **2014**, *47*, 1411–1478. [CrossRef]
32. Yue, Z.W.; Zhou, J.; Feng, C.; Li, A. Numerical investigation of the effect of holes on dynamic fracturing in multi-flawed granite. *Fatigue Fract. Eng. Mater. Struct.* **2021**, *44*, 1883–1896. [CrossRef]
33. Zou, C.J.; Wong, L.N.Y.; Loo, J.J.; Gan, B.S. Different mechanical and cracking behaviors of single-flawed brittle gypsum specimens under dynamic and quasi-static loadings. *Eng. Geol.* **2016**, *201*, 71–84. [CrossRef]
34. Li, X.B.; Zhou, T.; Li, D.Y. Dynamic strength and fracturing behavior of single-flawed prismatic marble specimens under impact loading with a split-Hopkinson pressure bar. *Rock Mech. Rock Eng.* **2017**, *50*, 29–44. [CrossRef]
35. You, W.; Dai, F.; Liu, Y.; Li, A. Numerical assessment of the rate-dependent cracking behaviours of single-flawed rocks in split Hopkinson pressure bar tests. *Eng. Fract. Mech.* **2021**, *247*, 107656.
36. Li, P.; Cai, M.F.; Gao, Y.B.; Wang, P.T. Dynamic mechanical behavior and cracking mechanism of cross-jointed granite containing a hole. *J. Mater. Res. Technol.* **2023**, *22*, 1572–1594. [CrossRef]
37. Tao, M.; Zhao, H.T.; Momeni, A.; Wang, Y.Q. Fracture failure analysis of elliptical hole bored granodiorite rocks under impact loads. *Theor. Appl. Fract. Mech.* **2020**, *107*, 102516. [CrossRef]
38. Zhao, R.; Tao, M.; Zhao, H.T.; Cao, W.Z. Dynamics fracture characteristics of cylindrically-bored granodiorite rocks under different hole size and initial stress state. *Theor. Appl. Fract. Mech.* **2020**, *109*, 102702. [CrossRef]
39. Zhou, X.; Xie, Y.J.; Long, G.C.; Zeng, X.H. Multi-scale modeling of the concrete SHPB test based on DEM-FDM coupling method. *Constr. Build. Mater.* **2022**, *356*, 129157. [CrossRef]
40. Li, X.B.; Zou, Y.; Zhou, Z.L. Numerical simulation of the rock SHPB test with a special shape striker based on the discrete element method. *Rock Mech. Rock Eng.* **2014**, *47*, 1693–1709. [CrossRef]
41. Pei, P.D.; Dai, F.; Liu, Y.; Wei, M.D. Dynamic tensile behavior of rocks under static pre-tension using the flattened Brazilian disc method. *Int. J. Rock Mech. Min. Sci.* **2020**, *126*, 104208. [CrossRef]
42. Yang, S.Q.; Yin, P.F.; Zhang, Y.C.; Chen, M. Failure behavior and crack evolution mechanism of a non-persistent jointed rock mass containing a circular hole. *Int. J. Rock Mech. Min. Sci.* **2019**, *114*, 101–121. [CrossRef]
43. Qiu, J.D.; Li, D.Y.; Li, X.B. Dynamic failure of a phyllite with a low degree of metamorphism under impact Brazilian test. *Int. J. Rock Mech. Min. Sci.* **2017**, *94*, 10–17. [CrossRef]
44. Li, Y.Z.; Dai, F.; Wei, M.D.; Du, H.B. Numerical investigation on dynamic fracture behavior of cracked rocks under mixed mode I/II loading. *Eng. Fract. Mech.* **2020**, *235*, 107176. [CrossRef]
45. Patel, S.; Martin, C.D. Impact of the initial crack volume on the intact behavior of a bonded particle model. *Comput. Geotech.* **2020**, *127*, 103764. [CrossRef]
46. Huang, Y.H.; Yang, S.Q.; Tian, W.L. Crack coalescence behavior of sandstone specimen containing two pre-existing flaws under different confining pressures. *Theor. Appl. Fract. Mech.* **2019**, *99*, 118–130. [CrossRef]
47. Koyama, T.; Jing, L. Effects of model scale and particle size on micro-mechanical properties and failure processes of rocks—A particle mechanics approach. *Eng. Anal. Bound. Elem.* **2007**, *31*, 458–472. [CrossRef]
48. Manso, J.; Marcelino, J.; Caldeira, L. Effect of the clump size for bonded particle model on the uniaxial and tensile strength ratio of rock. *Int. J. Rock Mech. Min. Sci.* **2019**, *114*, 131–140. [CrossRef]

49. Chen, M.; Zhang, Y.L.; Zhang, G.C.; Zhou, G.L. Discrete element study on mechanical response and pressure relief effect of rock containing variable hole. *Theor. Appl. Fract. Mech.* **2023**, *127*, 103976. [CrossRef]
50. Chen, M.; Yang, S.Q.; Ranjith, P.G.; Zhang, Y.C. Cracking behavior of rock containing non-persistent joints with various joints inclinations. *Theor. Appl. Fract. Mech.* **2020**, *109*, 102701. [CrossRef]

Disclaimer/Publisher's Note: The statements, opinions and data contained in all publications are solely those of the individual author(s) and contributor(s) and not of MDPI and/or the editor(s). MDPI and/or the editor(s) disclaim responsibility for any injury to people or property resulting from any ideas, methods, instructions or products referred to in the content.